Experimental study and modeling of cold-formed steel lipped channel stub beam-columns

S. Torabian[1], B. Zheng[2], B.W. Schafer[3]

Abstract
In this paper, the structural strength and stability of cold-formed steel lipped channel beam-columns under bi-axial moments and axial force is experimentally and numerically investigated. Seventeen 600S137-54 (AISI-S200-12 nomenclature) lipped channel stub column sections with a length of 305 mm [12 in.] are tested under combined bi-axial bending moments and axial force to characterize the member strength. The results are employed to evaluate the current AISI-S100-12 specification for strength predicting of beam-columns. The experimental results show a considerable potential for improvement in the current specification approach that utilizes a simple interaction equation. To extend the test results to the complete strength surface of the lipped channel section, and to understand the structural behavior of the beam-column more precisely, a series of geometric and material nonlinear shell finite element collapse analyses have been performed in ABAQUS. Modeling parameters including material σ–ε behavior, residual stresses and strains from cold-forming, and geometric imperfections; as well as, basic member properties including cross-section dimensions, member length, and boundary conditions are all considered. The developed model is validated against the experiments. Comparisons to current design methods indicate significant regions where an improved design method would allow engineers to realize significantly more strength in cold-formed steel beam-columns. The potential for further improvement of the current specification for predicting the strength of cold-formed steel beam-columns is discussed.

1. Introduction

Axial capacity and bending moment capacity of cold-formed steel structural members, e.g. lipped channels and Zee sections, have been studied extensively. Current design codes such as the North American Specification of the American Iron and Steel Institute (AISI-S100 2012) and the Australian/New Zealand Standard (AZ/NZS) for cold-formed steel structures (AS/NZS 2005)

---

[1] Postdoctoral Reseacrh Fellow, Department of Civil Engineering, Johns Hopkins University, <storabi2@jhu.edu>
 School of Civil Engineering, College of Engineering, University of Tehran, <torabian@ut.ac.ir>
[2] Visiting Student, Department of Civil Engineering, Johns Hopkins University, <bzheng3@jhu.edu>
 Ph.D. Student, School of Civil Engineering, Southeast University, Nanjing, 210096, China
[3] Professor and Chair, Department of Civil Engineering, Johns Hopkins University,<schafer@jhu.edu>

formally provide two design methods to determine the axial strength of columns and the flexural capacity of beams; the traditional effective width method (EWM), and the more recently developed direct strength method (DSM). The EWM takes into account the effect of plate local buckling by reducing each plate in a cross-section to its effective width, that in turn leads to the reduction of a gross cross-section to an effective cross section (via an iterative solution). On the other hand, DSM takes cross-section stability directly into account through a series of design strength equations driven by advanced computational analyses, such as the finite strip method, to determine the elastic buckling loads of the member in local, distortional and/or global modes of failure, including interactions.

Although extensive efforts have been devoted to determining the capacity of cold-formed steel members under pure axial or flexural actions, the design of structural members including a combination of actions has seen less study. Instead, design under combined actions, e.g. in AISI-S100-12 for both EWM and DSM, is developed as a simple linear combination of the isolated pure axial or flexural design previously studied. Stability, particularly local and distortional buckling, is directly tied to the stress distribution developed over the cross-section under the combined actions. Current cold-formed steel beam-column design does not determine stability under the actual combined actions, and ignores any nonlinear interaction in the strength between axial load and bending.

In this study, the structural strength and stability of cold-formed steel lipped channel beam-columns under bi-axial moments and axial force is experimentally and numerically investigated. Potential improvements in the current specification approach, that utilizes a simple interaction equation for beam-column strength prediction, are sought. Seventeen short 600S137-54 (AISI-S200-12 nomenclature) lipped channel sections with a length of 305 mm [12 in.] are tested under combined bi-axial bending moments and axial force. The combined axial force and bi-axial bending moments were applied via a custom test rig designed to apply axial load with eccentricities. To complement the limited combination of experimentally investigated axial force and bi-axial bending moments, geometric and material nonlinear shell finite element collapse analyses were performed in ABAQUS (Simulia 2013). The models extend the test results to a complete strength surface and provide a more precise understanding of the structural behavior under combined actions.

The presented results are a part of an ongoing comprehensive study developing a new explicit DSM prediction for cold-formed steel beam-columns. This larger effort includes additional tests on 600S137-54 lipped channel sections at a length of 610 mm [24 in.] and 1220 mm [48 in.] and also cold-formed steel Zee sections. In addition a new design formulation and complementary numerical analyses are also underway. The short length, 305mm [12 in.] specimens, considered here largely mobilize local modes of failures and thus this mode under combined actions is the primary focus of this paper.

2. Experimental Program

2.1 Normalized P-M₁-M₂ Space

A dimensionless normalized coordinate system in P-M_1-M_2 space is implemented to define the state of the applied combined actions including bi-axial bending moments (M_1, M_2) and axial force (P) with respect to the corresponding yield strength as following (also see Fig.1),

$$x = \frac{M_1}{M_{y1}} \tag{1}$$

$$y = \frac{M_2}{M_{y2}} \tag{2}$$

$$z = \frac{P}{P_y} \tag{3}$$

where, M_1 and M_2 are two orthogonal (mostly principal) axes of the cross section and the denominators (subscript y) are the corresponding yield moments (force).
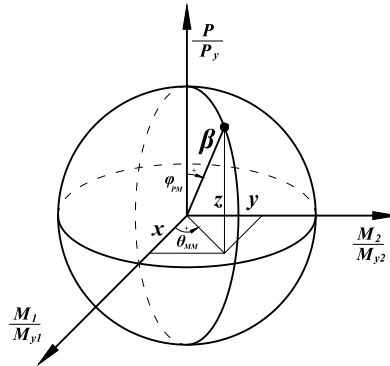
Figure 1:Normalized P-M₁-M₂ Space

Points in the normalized P-M_1-M_2 space are defined by an azimuth angle, θ_{MM}, an elevation angle, ϕ_{PM}, and a radial length β:

$$\theta_{MM} = \tan^{-1}(y/x) \tag{4}$$

$$\phi_{PM} = \cos^{-1}(z/\beta) \tag{5}$$

$$\beta = \sqrt{x^2 + y^2 + z^2} \tag{6}$$

The normalized axial and bending moment strength of a member are just anchor points on the x, y, and z axes. Connecting all the points corresponding to the strength of a member associated with a particular θ_{MM} and ϕ_{PM} angles results in the strength surface of a member in 3D space. In this study, axis 1 is assumed to be the major axis of the lipped channel section "axis z" in the

physical tests (see Fig. 4); and axis 2 is assumed to be "axis *x*" in the physical tests (see Fig. 4). The use of a generalized coordinate system is more important in the development of new explicit design methods, part of the aforementioned larger project but not the focus here; however, it is introduced here so that all results are in a common format.

2.2 Test Matrix

Building a 3D *P-M₁-M₂* interaction surface requires many tests. Given the time and expense with testing only a limited number may be completed. Therefore, a single cross-section under a large variety of *P-M₁-M₂* loading conditions is tested. The selected cross-section is the 600S137-54 (F_y=345MPa [50 ksi]). The length of the specimen is 305 mm [12 in.] to isolate global buckling and primarily mobilize local and/or distortional buckling. The distortional buckling half-wavelength is less than 305 mm [12 in.] and the specimen has warping fixed ends, thus distortional buckling is significantly boosted above its simply-supported lower bound (signature curve) value and local buckling is generally the primary behavioral mode.

Based on the defined dimensionless parameters in *P-M₁-M₂* space, 17 uniformly distributed test specimens are considered. As tabulated in Table 1, 9 specimens are considered for principal axes bending, including when the minor axis lip is in tension (θ_{MM}=270°), and when the minor axis lip is in compression (θ_{MM}=90°), as well as major axis (θ_{MM}=0°) bending. Moreover, 8 other specimens are considered in four other non-principal axes that are for bi-axial bending and axial force (θ_{MM}=30°, 60°, 300°, 330°). The equivalent physical eccentricities are also tabulated in the test matrix table (see Fig. 4 for axes definitions).

Table 1: Test Matrix

No.	Specimen in testing	Target				Measured					
		Eccentricities		Angles		Provided eccentricities				Angles	
		e_x	e_z	θ_{MM}	ϕ_{PM}	e_x	e_{zB0}	e_{zT0}	$e_{z\text{-Average}}$	θ_{MM}	ϕ_{PM}
		(in.)	(in.)	(deg.)	(deg.)	(in.)	(in.)	(in.)	(in.)	(deg.)	(deg.)
1	S600-12-1	0.00	-1.00	**270**	**79**	0.00	-1.077	-1.073	-1.075	**270.0**	**79.8**
2	S600-12-19	0.00	-0.50	**270**	**69**	0.00	-0.543	-0.538	-0.541	**270.0**	**70.4**
3	Minor axis S600-12-4	0.00	-0.15	**270**	**38**	0.00	-0.191	-0.178	-0.185	**270.0**	**43.8**
4	bending S600-12-5	0.00	0.15	**90**	**38**	0.00	0.102	0.115	0.109	**90.0**	**29.4**
5	S600-12-6	0.00	0.35	**90**	**61**	0.00	0.304	0.311	0.308	**90.0**	**58.0**
6	S600-12-8	0.00	1.00	**90**	**79**	0.00	0.973	0.927	0.950	**90.0**	**78.5**
7	Major axis S600-12-9	-1.00	0.00	**0**	**31**	-1.00	-0.017	-0.068	-0.043	**340.1**	**33.0**
8	bending S600-12-10	-3.50	0.00	**0**	**65**	-3.50	-0.010	-0.016	-0.013	**358.2**	**65.0**
9	S600-12-11	-7.50	0.00	**0**	**78**	-7.50	-0.003	0.005	0.001	**360.0**	**77.7**
10	S600-12-2	-1.50	0.1019	**30**	**47**	-1.50	0.107	0.107	0.107	**31.1**	**47.0**
11	S600-12-13	-5	0.3397	**30**	**74**	-5	0.333	0.343	0.338	**29.8**	**74.2**
12	S600-12-14	-0.813	0.1656	**60**	**45**	-0.813	0.172	0.160	0.166	**60.1**	**44.9**
13	Bi-axial S600-12-15	-3	0.6115	**60**	**75**	-3	0.637	0.620	0.628	**60.7**	**75.1**
14	bending S600-12-16	-0.813	-0.1656	**300**	**45**	-0.813	-0.158	-0.163	-0.161	**300.8**	**44.2**
15	S600-12-17	-3	-0.6115	**300**	**75**	-3	-0.615	-0.612	-0.614	**299.9**	**74.8**
16	S600-12-3	-1.5	-0.1019	**330**	**47**	-1.5	-0.095	-0.105	-0.100	**330.5**	**46.5**
17	S600-12-20	-5	-0.3397	**330**	**74**	-5	-0.338	-0.335	-0.337	**330.2**	**74.2**

1 in. = 25.4 mm

The specimens are grouped into minor (no. 1-6), major (no. 7-9) and bi-axial (no. 10-17) bending loading conditions, per Table 1. Moreover, each specimen has a designation of S600-12-X, where the 600 and the 12 indicate the depth and the length of the specimen and X is a sequential number assigned before testing.

Table 1 provides targeted angles and eccentricities and also the actual eccentricities measured at the top and bottom of the specimen before loading. Notably, in the larger testing program two other lengths are also considered for testing: 1219 mm [48 in.] (local-global and distortional modes) and 610 mm [24 in.] (mixed buckling modes and also distortional buckling). The testing program for other lengths and other cross-sections, particularly *Zee* sections, is underway.

2.3 Test specimens, preparation and material testing

To provide a uniform stress distribution along the length of the specimen combined compressive axial load and constant moment distribution was considered as a baseline for the beam-column response. Constant stress along the length is consistent with typical theoretical plate stability solutions and the basic assumptions of the semi-analytical finite strip method (FSM). FSM is often utilized to investigate the elastic stability of cold-formed steel members, including local and distortional buckling.

There are several ways to provide constant moment distribution in a beam-column test: four point transverse loading, eccentric loading, end-moment loading, etc. However, applying eccentric loading is one of the simplest and most practical. Four point transverse loading must always consider torsional moments induced by the transverse loads not passing through the lipped channel shear center; and end-moment loading typically requires an involved test setup. Eccentric loading can provide uniform bi-axial bending moments with warping restraint for the ends. Where a pin-pin end condition is needed at the point of loading, a simple (single actuator) compressive loading rig can be used to apply the eccentric load.

As shown in Fig. 3 and 4, the test specimens were lipped channels with welded end plates. The welded plates at the ends of the specimen provide warping fixed restraints and enable the specimen to be adjusted in the rig and clamped to the loading plates. To estimate the realistic shape of the test specimen cross-section dimensions such as depth (*H*), flange width (*B*), lip length (*d*) and the corner angles and radii were measured before welding. The ends of the channel specimens were also milled flush before welding to ensure flatness. A custom welding jig was utilized to insure square-ness. To ensure welding quality and also to avoid poisonous materials produced during welding of the galvanized steel, the zinc coating of the test specimens was stripped by Hydrochloric (HCL-1N) acid. The welding electrode was ER70S-2 (482 MPa [70 ksi]) and a TIG welding system using GTAW welding process (Argon shield gas) was utilized to weld the specimens. To avoid end plate thermal bending during the welding, the weld leg size was kept at a minimum. Welding of the lips was especially inspected to ensure a complete and sound welded connection between the specimen and the end plate. These procedures were all in an effort to minimize the effect of end condition imperfection on the response.

To determine the material properties of the test specimens, 21 coupon samples were taken from both the initial coil and the final cold-formed beam-column specimens. To study the effect of zinc coating on the tensile strength and behavior of galvanized steel, three coupons were tested without zinc coating. The rest of the coupons were tested with coating, but the coating at the ends of the coupons was stripped to determine the zinc coating thickness (See Fig. 2). Rough-cut samples were taken from central parts of the channel web and the flange. CNC cutting was

utilized for machining out the desired shape of the test specimens. Comparison of coupons from the member flats and the original coil, and coated versus un-coated specimens, revealed that neither roll-forming or the zinc-coating have significant effects on the yield and ultimate strength of the specimens. Accordingly, an averaged engineering stress-strain curve (σ_E-ε_E) is provided in Fig. 2 along with the averaged yield and ultimate strength of the material. To enable use of the material testing results in the numerical analyses, a 23-point material model is adopted (σ_{Ei}-ε_{Ei}) and converted to true-stress strain results (σ_T-ε_T) as shown in Fig. 2.
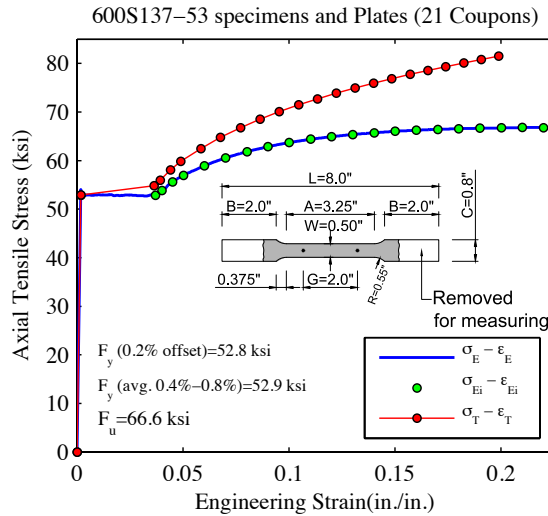
Figure 2: Tensile test results (1 ksi=6.8948 MPa)

2.3 Test setup and Instrumentation and the loading equipment

A new test rig was designed for performing the beam-column tests within a uniaxial 445 kN [110 kip] MTS loading frame in the Thin-Walled Structures Laboratory at Johns Hopkins University. As shown in Fig. 3, the loading rig consists of top and bottom MTS standard swivel joints for applying compressive force and providing pin-pin end-restraints for the beam-column specimen, two loading plates to accommodate eccentricity in both axes, required clamps, instrumentation, and a data acquisition system.

The clamps (Fig. 3) provide compressive bearing stress between the welded end plates and the loading plate to prevent uplift and detachment. The clamping mechanism enables the test rig to be used for all beam-column specimens in the project. To adjust the top and bottom loading plate, hanging bolts and sitting bolts, which were connected to the external Frazier rack frame, are provided as shown in Fig. 4. These bolts are removed before testing. As shown in Fig 3(b), the Frazier rack frame (external frame with blue columns and orange beams) is a supporting frame placed around the MTS universal testing rig to provide support for the loading plates and instrumentation.
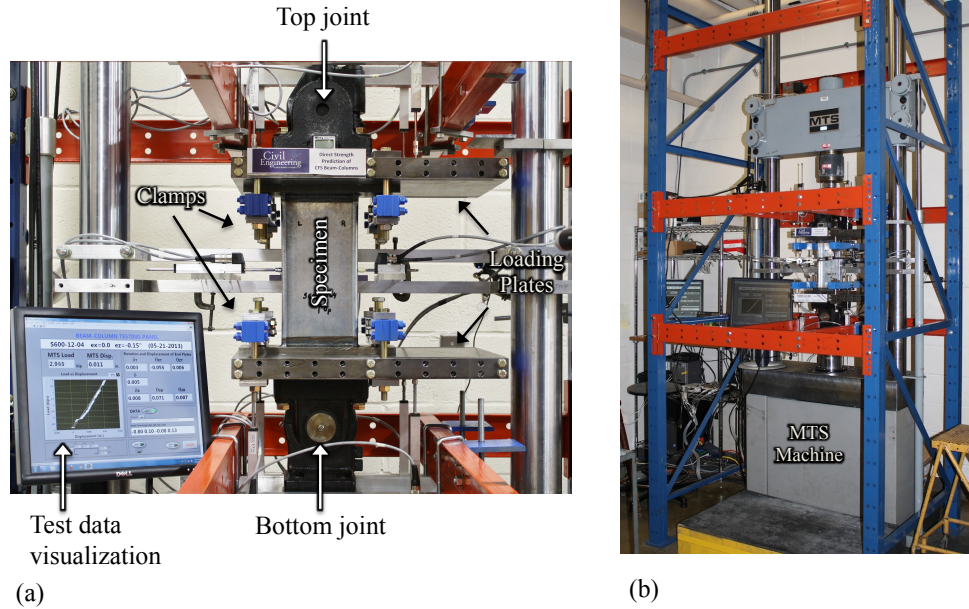
Figure 3:Test setup of the beam-column experimental program. (a) Loading plates and swivel joints, (b) Test specific facilities including MTS machine (100 kips), Frazier Rack and the test rig.

The beam-column test setup was equipped with a series of position transducers (PTs) to record the displacements and rotations of the end plates and the specimen throughout the experiments. All position transducers are routed to a NI-6024 PCI card for reading and monitoring of the results via LabView. An MTS407 controller drove the actuator displacements and recorded the applied displacement via an internal LVDT installed in the actuator; and the force via a load cell connected to the crosshead. Both force and displacement transducers were routed to the PCI card via the MTS407 and monitored in LabView.

All mounted instrumentations are illustrated in Fig. 4. As shown in the figure, four position transducers (PT1 to PT4) were utilized to record bottom plate rotations and displacements (see section A-A in Fig.4) and four other PTs (PT5 to PT8) are utilized to capture the rotations and displacements of the top plate (see section C-C in Fig. 4). Seven other PTs were mounted to record the movements and deformations of the specimen at mid-height, as shown in section B-B in Fig. 4. These PTs measured the cross-section movements at 7 points including both flanges and the web. The results are used to calculate several parameters such as mid-height displacements in x and z axes (see Fig. 4 for axes definition), rigid-body rotation of the specimen, flange local rotations in distortional buckling, and web local buckling. To provide enough flexibility in mounting, PTs were connected on Plexiglas sheets and clamped to the mounting beam; and then routed to the data acquisition systems.

2.4 Specimen placing and testing procedure

Setting the specimens in the test rig was the most important part of the testing program that could directly affect the test results. The main purpose of the setting procedure was to place the specimen at the targeted eccentricity considered for each specimen per Table 1.
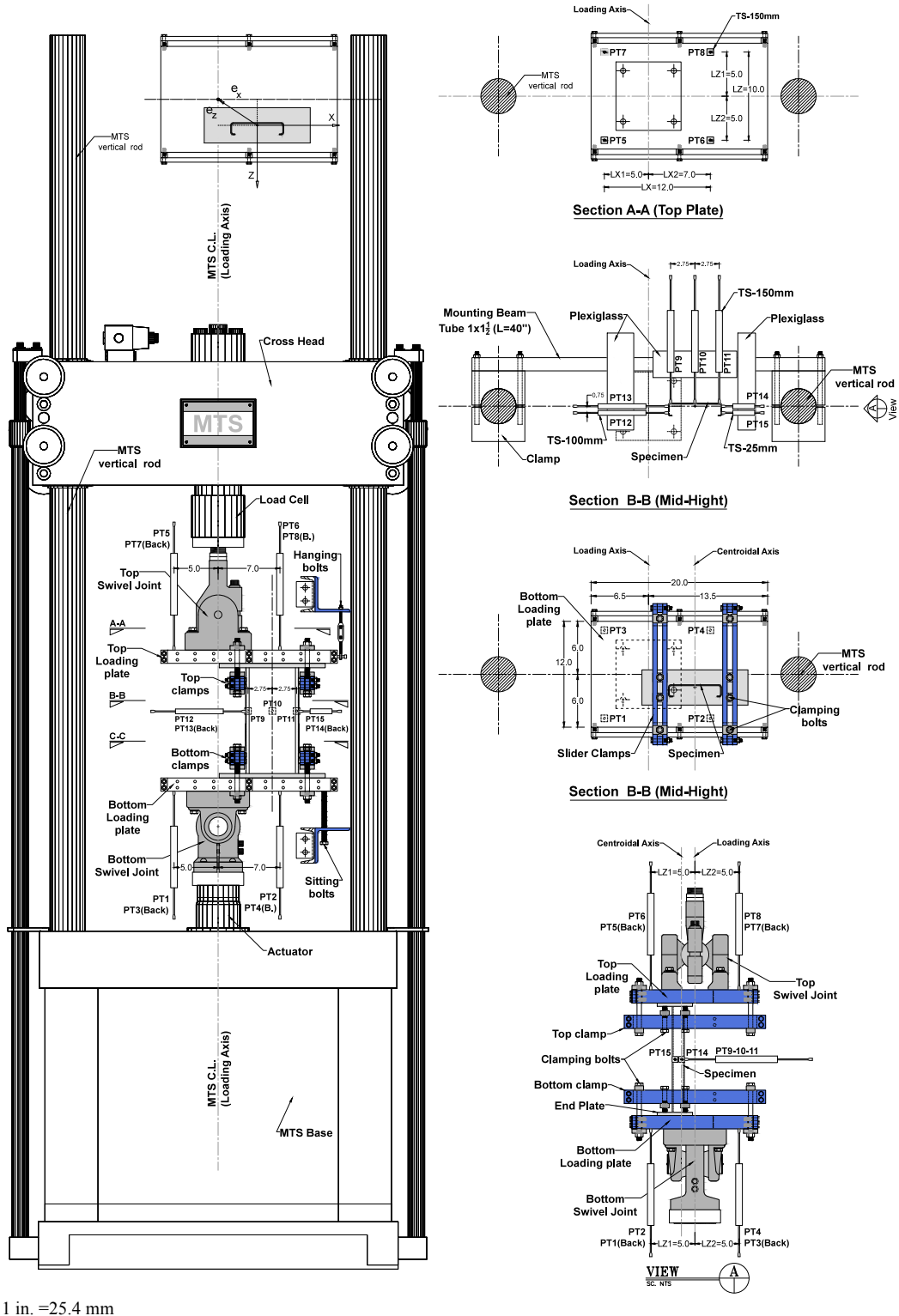
Figure 4: Test Setup and instrumentation configuration for beam-column experiments (PT: Position Transducer)

Each specimen should be placed at a defined distance to the load point along both "*x-*" and "*z-*axis". To precisely measure the position of the specimen, two precise reference measuring beams

were provided in the test rig as illustrated in Fig. 5. It should be noted that in most cases specimens are not perfectly perpendicular to the end plates. The rotational capabilities of the swivel joints accommodate these initial end angles, and the initial end angles are recorded. Direct measuring of the eccentricities to an external reference ensured the accuracy of the load position on the cross-section. The measured eccentricities are tabulated in Table 1. After placing the specimens, all tests were performed in displacement control with a proper (pseudo-static) loading rate (typically 0.0635 mm/sec. [0.0025 in./sec]) until the maximum load capacity and then continued to about 80% of the maximum load before stopping the test.
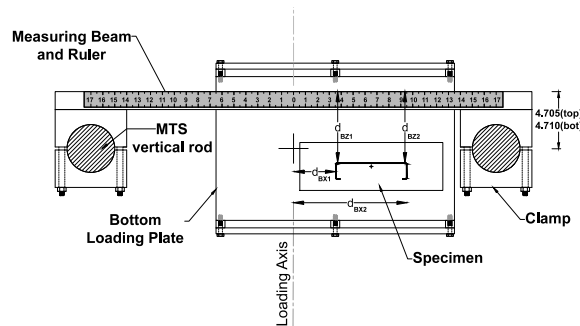
Figure 5: Setting the specimens in the test rig (bottom measuring beam)
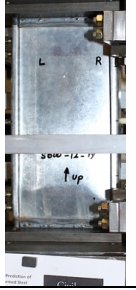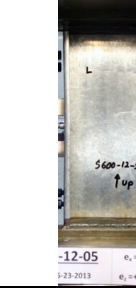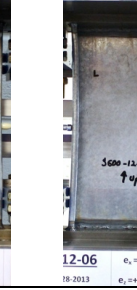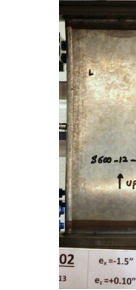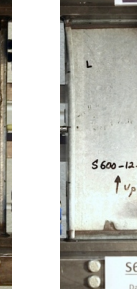
2.5 Test results and observations

As shown in Table 2(a), three specimens were tested with negative eccentricities in minor axis, or negative minor axis bending, (no. 1-3) providing tension on the lips and three other specimens (no. 4-6) were tested with positive eccentricities providing compression on the lips (positive minor axis bending). The characteristic observed failure mode of the first three specimens was web local buckling (WLB) followed by consistent flange deformations in the final post-peak stages. Flange deformations were relatively small and happened late compared to the web deformations. Axial load and minor axis bending with negative eccentricity applies compressive stresses on the web and tensile stresses on the flanges and the lips – it is expected that the web buckling dominates, while the lips are stabilized under tensile stresses. For the specimens in minor axis bending with positive minor axis eccentricities (no. 4-6), as expected, the compressive stress causes flange distortional buckling (FDB) in almost all cases, as shown in Table 2(a). Following the flange buckling, a consistent web deformation was observed in all three tests. The specimens with smaller eccentricities behaved more like columns. Accordingly, a mixed local and distortional buckling is observed in Specimen 4 with the smallest positive eccentricity in the minor axis (z-direction).
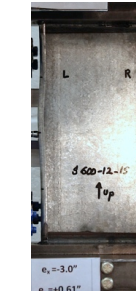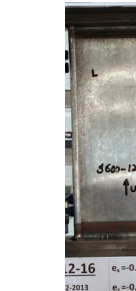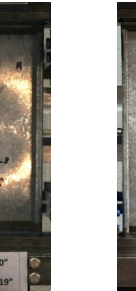
Table 2(b) summarizes the results of the experiments on the beam-columns under axial loads and major axis bending. Typically in the "left flange" (flange with compression from major axis moment) distortional buckling was the main characteristic failure mode, while in all cases a consistent web local buckling was also observed. Specimen 7, with the smallest eccentricity in the major axis, experienced more severe web local buckling than the "left flange" distortional buckling. Given the relatively high level of axial load in this specimen, the tested beam-column is more like a column and the uniform axial stress on the cross-section is enough to mobilize the

9

web local buckling. However, mostly in the post-peak stage, the major bending of the specimen caused distortional deformations in the left flange.

Table 2: Test results: Stub beam-columns

(a)	Minor axis bending: (-) minor bending			Minor axis bending: (+) minor bending		
θ_{MM} ($\theta_{MM\text{-target}}$)	270° (270°)	270° (270°)	270° (270°)	90° (90°)	90° (90°)	90° (90°)
ϕ_{PM} ($\phi_{PM\text{-target}}$)	79.8° (79.0°)	70.4° (69°)	43.8° (38°)	29.4° (38°)	58.0° (61°)	78.5° (79°)
Test Specimen at the failure load						
P_{max} kN [kips]	(LIT, WLB) 25.38 [5.706]	(LIT, WLB) 41.37 [9.3]	(LIT, WLB) 55.6 [12.5]	(LIC,FDB/WLB) 72.05 [16.2]	(LIC, FDB) 50.26 [11.30]	(LIC, FDB) 26.11 [5.87]

(b)	Major axis bending			Bi-axial bending: (+) minor bending	
θ_{MM} ($\theta_{MM\text{-target}}$)	340.1° (360°)	358.2° (360°)	360° (360°)	31.1° (30°)	29.8° (30°)
ϕ_{PM} ($\phi_{PM\text{-target}}$)	77.7° (78°)	65° (65°)	31° (33°)	47.0° (47)	74.2° (74°)
Test Specimen at the failure load					
P_{max} kN [kips]	(WLB) 54.31 [12.21]	(WLB) 31.40 [7.06]	(WLB) 20.55 [4.62]	(FDB/WLB) 48.93 [11.0]	(FDB) 21.26 [4.78]

(c)	Bi-axial bending: (+) minor bending		Bi-axial bending: (-) minor bending			
θ_{MM} ($\theta_{MM\text{-target}}$)	60.1° (60°)	60.7° (60°)	300.8° (300°)	299.9° (300°)	330.5° (330°)	330.2° (330°)
ϕ_{PM} ($\phi_{PM\text{-target}}$)	44.9° (45°)	75.1° (75°)	44.2° (45°)	74.8° (75°)	46.5° (47°)	74.2° (74°)
Test Specimen at the failure load						
P_{max} kN [kips]	(LIC,FDB) 52.53 [11.81]	(FDB) 25.0 [5.62]	(WLB) 48.04 [10.8]	(WLB) 26.51 [5.96]	(WLB) 48.26 [10.85]	(WLB) 24.95 [5.61]

The remaining specimens are beam-columns under axial load and bi-axial bending. Four specimens have been tested assuming positive eccentricity in the minor axis (no. 10-13) and four other specimens (no. 14-17) were tested by providing negative eccentricity in the minor axis. Positive eccentricity in the minor axis causes compressive stresses in both the flanges and lips.

Therefore, two sources of compressive stresses were on the left flange, one from the minor axis bending and the other from the major axis bending, making the flange distortional buckling the main failure mode for all four specimens at $\theta_{MM}=30^{\circ}$ and 60°. However, for the specimen with the smaller eccentricity, higher axial load on the specimen mobilized web local buckling as well. It is hypothesized that the different failure shapes of the specimens, shown in the table, can be justified by the different pattern of distortional imperfection.

The test results for the beam-column specimens under bi-axial bending including negative eccentricity in the minor axis are presented in Table 2(c). At $\theta_{MM}=300^{\circ}$ and 330° the observed failure mode for both tested specimens was web local buckling and distortion of the flanges was not remarkable compared to the web local buckling. The results showed that the slender web of the cross-section governed the failure modes of the member and even a small eccentricity causing more compression on the slender web can mobilize web local buckling.
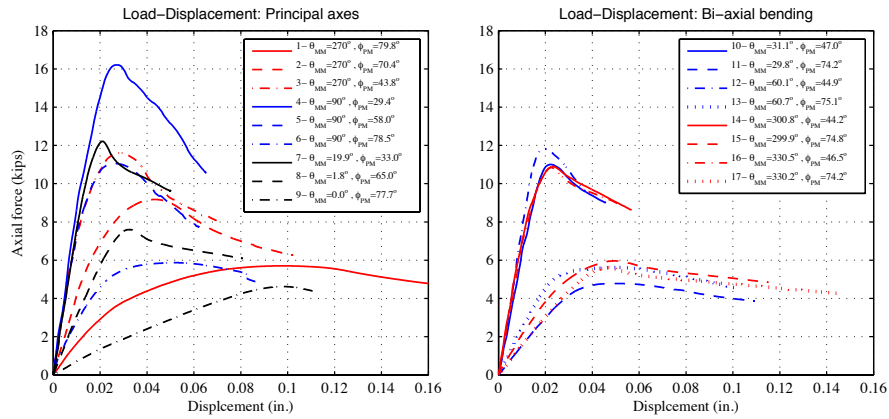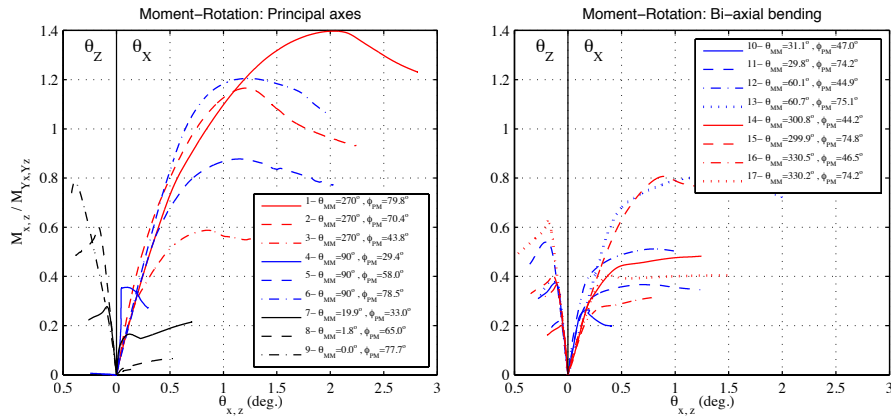

Figure 6: Test results: Load vs. displacement.

Figure 7: Test results: End moment vs. end rotation (averaged absolute values; 1 kip=4.448 kN).

According to the test results (see Fig. 6), the more the "beam-column" is close to the "beam" assumption, the more ductility and inelastic-reserve are provided. On the other hand, when the "beam-column" is close to "column" characteristics, less ductility and steeper post-peak strength degradation is expected. The load-displacement curve of the specimens with small negative minor eccentricity also shows a more "brittle" failure compared to the other specimens with larger eccentricities. The small minor axis moment associated with minor-axis eccentricity could

not overcome the axial stress on the cross-section and all elements including the web and the flanges were essentially in compression at the peak load. As shown in Fig. 7, M_{minor}-θ_{Minor} moment rotations curves typically exhibit "ductile" response, but all M_{major}-θ_{major} moment rotations curves are more of a "brittle"-type response. Values in Fig. 7 are the average of the top and the bottom moments and rotations. Moreover, the left hand side of the figure is the rotation around "axis z" (major axis bending) and the right hand side of the figure is the rotation around "axis x" (minor axis bending). Although the web local buckling resulted in a less ductile failures and the flange distortional buckling typically provided more ductility (observed qualitatively in load-displacement and moment-rotation results), the member ductility was weakly correlated to the direction of the minor axis bending (positive or negative eccentricities). However, it is found that the member ductility is strongly correlated to the level of axial force and the axis of bending (major versus minor).

2.6 Comparison to AISI-S100-2012

As shown in Figs. 9 and 10, the experimental results are compared to the predictions of the newly developed AISI-S100-12 specifications by utilizing the DSM method for nominal axial (P_n) and flexural (M_{nx}, M_{ny}) strengths in Appendix 1; and the interaction equations in AISI-S100 section C5.2: Combined Compressive Axial Load and bending. Accordingly, the following interaction equation

$$\frac{\overline{P}}{\phi_c P_n} + \frac{C_{mx}\overline{M}_x}{\phi_b M_{nx}\alpha_x} + \frac{C_{my}\overline{M}_y}{\phi_b M_{ny}\alpha_y} \leq 1.0 \qquad (7)$$

where, $\overline{P}$, $\overline{M}_{x,y}$ are the required strengths, P_n, $M_{nx,ny}$ are the nominal strengths, $C_{mx,my}$ are moment gradient coefficients, $\alpha_{x,y} = 1 - \overline{P}/P_{Ex,y}$ is the P-δ moment amplification factors, $P_{Ex,y} = \pi^2 EI/(K_{x,y}L_{x,y})$ are the Euler buckling loads, and $\phi_{c,b}$ are compressive and bending resistance factors. Notably, z and x axes in the experimental study are assumed to be equivalent to x and y axes in Eq. 7.

Nominal strengths, were determined in accordance with the AISI-S100-12 Appendix 1 DSM method including inelastic reserve. Critical elastic local and distortional buckling axial load and moments were determined by CUFSM 4.06 finite strip program (Schafer and Adany 2006). To automatically identify local and distortional buckling a newly proposed method called "FSM@cFSM-L_{cr}" was used (Li and Schafer 2010). "FSM@cFSM-L_{cr}" utilizes a straight-line cross-section definition to perform a constrained finite strip method (cFSM) analysis to determine local and distortional buckling loads and the corresponding half-wave lengths (L_{cr}). Knowing L_{cr} for both local and distortional buckling, FSM can be utilized to determine the signature curve of the rounded-corner model. Local and distortional buckling loads at the associated L_{cr} are determined from the signature curve. Critical elastic column buckling and lateral-torsional beam buckling loads were determined from CUTWP (Sarawit 2006). Where the ends moments on the specimens were almost equal and the member was bent in single curvature, $C_{mx,my} = 1.0$; and to compare with the test results resistance factors were assumed to be unity

($\phi_{c,b} = 1.0$). Moreover, moment amplification factors ($\alpha_{x,y}$) were assumed to be 1.0, where the end-moment experimental results were compared to the specification predictions in Figs. 9 and 10.
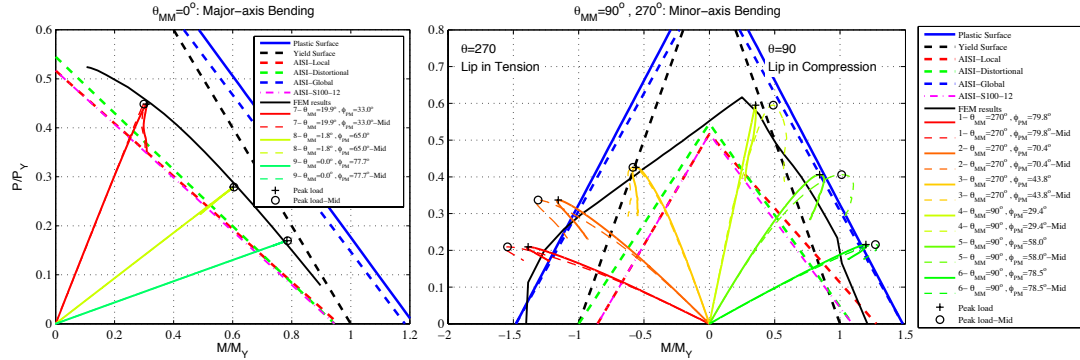

Figure 8: Test results vs. AISI-S100-12 prediction and FEM results in principal axes
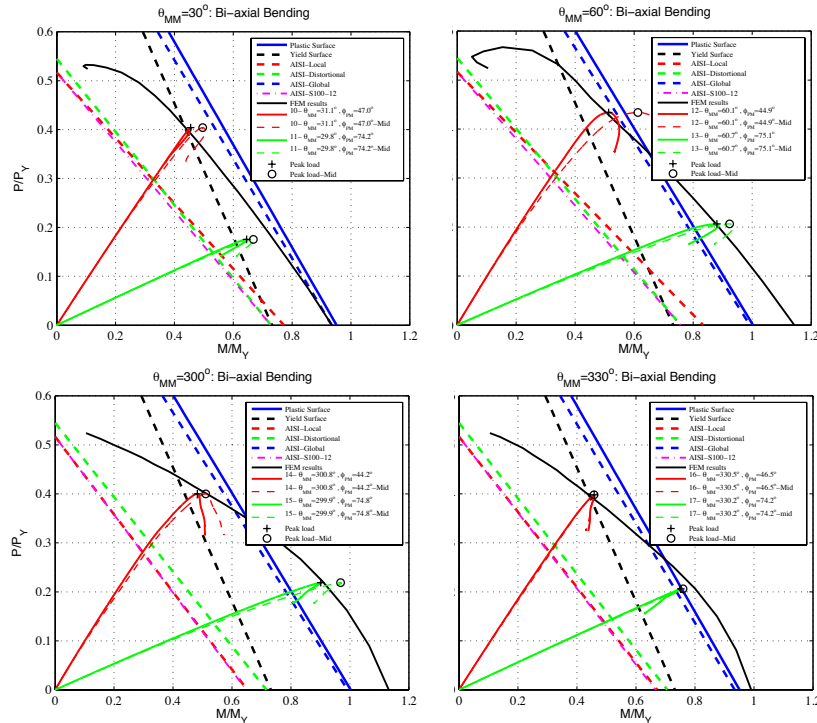

Figure 9: Test results vs. AISI-S100-12 prediction and FEM results in non-principal axes

For the DSM predictions, a correction was made to the distortional elastic buckling loads to address the actual clamped boundary conditions in the test rig. Clamped boundary conditions increase both the local and distortional elastic buckling loads; however, the increase in local buckling critical load is negligible. For distortional buckling in short members this increase may be large, particularly when the distortional buckling half-wave length (L_{crd}) is comparable to the length of the element. To account for this phenomenon, an empirical increase had been developed for boosting up the distortional buckling critical load (Moen 2008):

$$D_{boost} = 1 + \frac{1}{2}(\frac{L_{crd}}{L})^2 \qquad\qquad (8)$$

where, D_{boost} is the boosting factor for elastic distortional buckling load and L is the length of the member. Note, it is also possible to directly model the warping fixed end conditions in CUFSM 4.06; however, the signature curve does not exist in this case, and the results are slightly more complex – for simple design situations D_{boost} provides greater convenience. In the calculations L was assumed to be 305 mm [12 in.] for boosting up the distortional buckling; and 610 mm [24 in.] for global buckling calculations, where the length of the top and bottom rigid links must be included in the global length of the specimen between top and bottom pin joints.

The interaction curves at particular planes in P-M_1-M_2 space that include available experimental results are illustrated in Figs. 9 and 10. In each figure, all available numerical, analytical, and experimental results are compared together. To show the contribution of each of the limits states, the linear interaction equation (Eq. 7) was implemented to provide a distinct interaction curve for the several limit states: plastic limit, yield limit, global limit, distortional limit, and local limit.

Generally speaking, the AISI design method follows the experimental results, although it is quite conservative. AISI-S100-12 successfully predicted the failure mode of the specimens, although the results were quit conservative in terms of strength. All the specimens with negative minor axis bending (causing tension in the lips) failed in local buckling and all other with positive minor axis bending failed in the distortional mode. Most of the failures occurred beyond the yield surface and for some beyond the plastic surface indicating significant inelastic reserve. For almost all specimens the global plastic surface was close to the plastic surface indicating a high global buckling load (as desired) and minimal local-global interaction. As tabulated in Table 6, the average $\beta_{Test}/\beta_{n\text{-}AISI}$ is 1.51 and the associated C.O.V is 16%.

For each test the moments were calculated including the "e_x" and "e_z" eccentricities at the rigid end distances as well as with the additional P-δ moment due to mid-height displacements denoted with a "Mid" in the plots. The FE model (as discussed in the next section) is in excellent agreement with the test except for axial and minor-axis bending where both AISI-S100-12 interaction curves and FE predictions remain consistently conservative.

3. Numerical modeling

The experimental results can only explore a limited number of points out of the full P-M_1-M_2 strength interaction space. To extend the test results to the complete strength surface, and to better understand the structural behavior of the beam-column more extensively, geometric and material nonlinear shell finite element collapse analyses was performed in ABAQUS. Modeling parameters including material σ–ε behavior, residual stresses and strains from cold-forming, and geometric imperfections; as well as, basic member properties including cross-section dimensions, member length, and boundary conditions are all considered as described in the following sections. The model for the collapse analyses was verified against the test results and then used to generate predictions of the load capacity for beam-columns with different eccentricities, which were subsequently compared with the predictions of AISI-S100-12.

3.1 Modeling protocols

3.1.1 Geometric modeling and boundary conditions

Two types of geometric dimensions are considered for modeling: nominal and actual measured dimensions. The nominal geometric dimensions are the industry tabled values (SFIA 2012), and the actual geometric dimensions are those taken from direct measurements. Results of nominal and actual models are generally close together for these sections (Torabian et. al. 2013). Therefore, nominal cross-sectional dimensions are adopted for collapse analyses reported here.

The cross section model was first built in CUFSM. Eigen buckling analysis was conducted to generate the expected imperfection mode. This was then converted to a shell element model in ABAQUS (via an input file). The geometric imperfections are discussed in the following section.

The shell element, S9R5, was used in the finite element model. It has been shown that this element can provide accurate predictions for thin-walled structures, and is more economical than other alternatives: S4, S4R and S8R5 (Schafer et. al. 2010). Based on a mesh density study in (Torabian et. al. 2013), an efficient mesh density including 10 elements in the web, 2 elements in the flange and the lip, 4 elements in the corner and 20 element along the length was selected for the shell model (see Fig. 10).
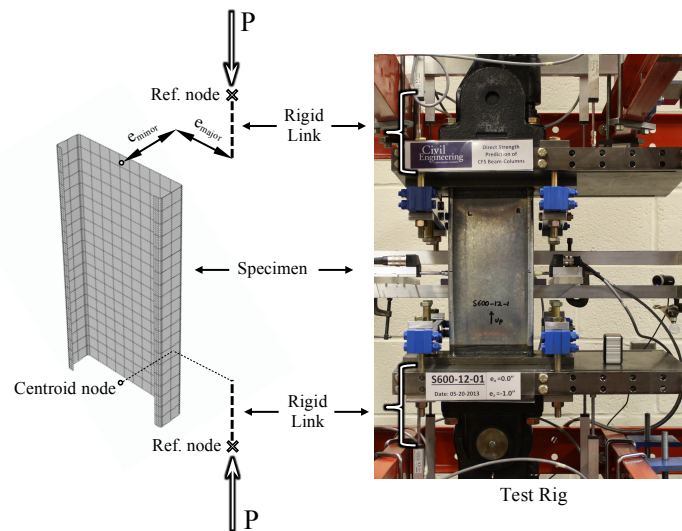

Figure 10: Finite element model: Geometric and boundary condition assumptions

Geometric and end boundary condition assumptions are summarized in Fig. 10. A reference node was considered at the center of the swivel joint at each end. The coordinate of the reference point varied as different eccentricities applied to the specimens. The nodal degrees of freedom at the end of the specimen were coupled to the reference point using a rigid body coupling. The length of the rigid link between the reference point and the end of the specimen was 6 inches in the longitudinal direction. At the supporting end (i.e. top ref. point), all the translational degrees of freedom and the torsional degree of freedom of the reference point were constrained. At the loading end (i.e. bottom ref. point), the reference point was constrained in a similar way, except

that the translational and rotational degree of freedom in the longitudinal direction were released. Concentrated force/displacement was applied at the reference point in the longitudinal direction.

3.1.2 Material properties and residual stress and strain

The plastic part of the true stress-true strain curve shown in Fig. 2 was used to define the multi-linear material property in ABAQUS. For the elastic part, the elastic Young's modulus, the yield stress and the Poisson's ratio were 2.03×10^5 MPa [29500 ksi], 365 MPa [53 ksi], and 0.3, respectively. The von Mises yielding rule, associated flow, and isotropic hardening were also adopted in the model.

The residual stress and effective plastic strain distribution model in Moen et. al. (2008) was used to consider residual stresses and the roll-forming effect. Due to the high yield stress 365 MPa [53 ksi] and the small thickness of the specimens 1.4376 mm [0.0566 in.], residual stresses and effective plastic strains in the flat region were ignored. Only the residual stresses and effective plastic strains in the corner regions were introduced into the finite element model. Fig. 11 shows the residual stresses and effective plastic strains used in modeling. Thirty-one through thickness integration points were used when the cold roll-forming effect were considered.
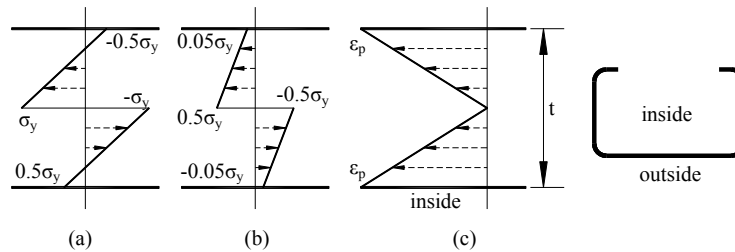

Figure 11: Residual stress and effective plastic strain in the corner regions
(a) residual stress in the transverse direction, (b) residual stress in the longitudinal direction,
(c) effective plastic strain, ε_p=0.26 (Moen et. al. 2008)

3.1.3 Geometric imperfections

Traditionally, buckling mode shapes are used as the imperfection distribution in collapse analyses. Three types of buckling modes are considered: local, distortional, and global. Typical buckling shapes of a lipped channel section in pure compression are shown in Fig. 12. For short members (like the specimens tested herein), the global mode of failure is not the governing mode; and only the local buckling mode and/or distortional buckling mode imperfection must be introduced into the perfect model. For longer specimens, which fail in interactive buckling, a combination of local and/or distortional, and/or global buckling mode imperfections must all be introduced into the perfect model.

The imperfection sign and the combination of the imperfection patterns are also important. For the local buckling mode and distortional buckling mode, the sign of the imperfection may imply flange buckling inward or outward. For global (weak-axis flexural) buckling, the sign of the imperfection may imply lips in tension or lips in compression. To provide a uniform imperfection pattern, the buckling modes used for the imperfection distribution are all from the axial compression mode of failure. Four combinations of the imperfection patterns in local and

distortional modes were also considered: (+)Local (+)Distortional, (+)Local (−)Distortional, (−)Local (+)Distortional, (−)Local (−)Distortional. Finally, two sympathetic buckling modes, (−)Local (−)Distortional, were selected based on a parametric study of the collapse strength. However, it was found that the results are not overly sensitive to the sign of imperfection (see (Torabian et. al. 2013) for more details).

The magnitude of the imperfection has been studied in Zeinoddini and Schafer (2012). The imperfection magnitude corresponding to 25%, 50% and 75% probability of exceedance (CDF values) for all buckling shapes are tabulated in Table 3. These magnitudes were used in validation of the finite element model. The imperfection magnitudes corresponding to the 50% CDF were used in this paper (also see Torabian et. al. 2013). It should be noted that the distribution, magnitude, and sign of the imperfection are firmly related to the manufacturing of the specimens. So these parameters may vary along with different batches of specimens and the method utilized here provides mathematical convenience, as much as physical reality.
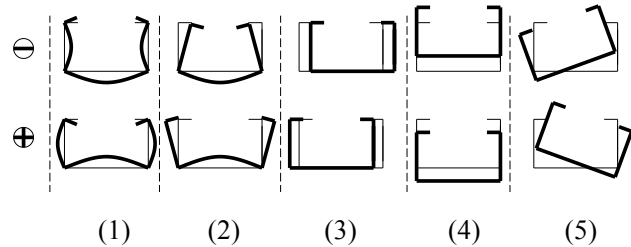

Figure 12: Typical buckling modes of lipped channel sections
(1) Local, (2) Distortional, (3) Global-Camber, (4) Global-Bow, (5) Global-Twist

Table 3: Imperfection magnitude (Zeinoddini and Schafer 2012)

CDF	Local (δ/t)	Distortional (δ/t)	Bow (L/δ)	Camber (L/δ)	Twist (Deg./m)
25%	0.17	0.43	4755	6295	0.20
50%	0.31	0.75	2909	4010	0.30
75%	0.54	1.14	1659	2887	0.49

3.2 Comparison to test results and validating

The arc-length method (Riks) was selected to perform geometric and material nonlinear shell finite element collapse analyses in ABAQUS. The FEM results are compared to the test results for validation in the following sections, and also compared to AISI-S100-12 for exploring the current linear interaction beam-column design equations.
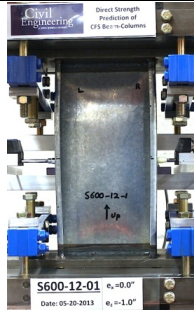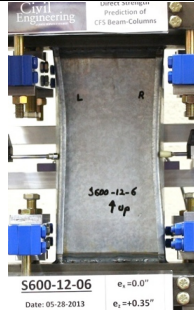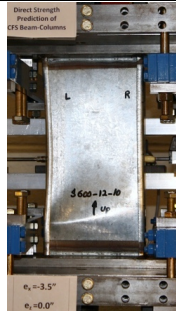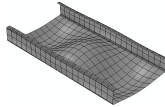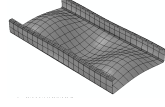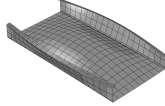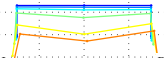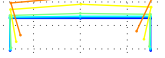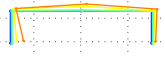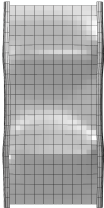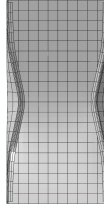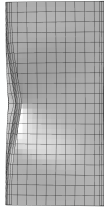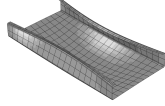
3.2.1 Failure modes

The observed failure modes and the recorded deformed shape of the tested specimens at mid-height are compared to the failure shape of the specimens in finite element analyses as shown in Tables 4 and 5 for principal and non-principal axes, respectively.

Each of the presented specimens is selected from a group of specimens that are expected to have the same behavior and buckling mode of failure. As shown in Tables 4 and 5, the selected

buckling shape (50% negative local, and 50% negative distortional buckling magnitude) provided consistent simulated buckling shapes in the FEM analyses. Due to the mathematical symmetry of the FEM models, all failure modes are symmetric about the mid-height of the specimens. However, the actual imperfection pattern of the specimens and the limitation and restraints of the physical testing often caused unsymmetrical modes of failure, also see Table 2.

Table 4: Failure modes in principal axes

	Minor axis bending		Major axis bending	Imperfection pattern in FEM analysis
	Lip in tension	Lip in compression		
	$\theta_{MM}=270^{o}$, $\phi_{PM}=79.8^{o}$	$\theta_{MM}=90^{o}$, $\phi_{PM}=58.0^{o}$	$\theta_{MM}=1.8^{o}$, $\phi_{PM}=65^{o}$	
Experiment / Deformed Shaped	S600-12-01 e_x=0.0" Date: 05-20-2013 e_z=-1.0"	S600-12-06 e_x=0.0" Date: 05-28-2013 e_z=+0.35"	e_x=-3.5" e_z=0.0"	Positive local buckling (L+)
	WLB	FDB	FDB	Negative local buckling (L-)
				Positive Distortional buckling (D+)
FEM				Negative Distortional buckling (D-)
	(L-) (D-)	(L-) (D-)	(L-) (D-)	

3.2.2 Initial stiffness

Comparing the initial stiffness of the tested specimens to the FEM models provides a check on the models and the testing as it can be an indicator of how precise the specimens were set in the test rig at the desired eccentricities as well as estimate the existence of slack in the clamping of the end plates and swivel joints. Change in the provided eccentricities can meaningfully change the initial stiffness of the specimens. Minor detachment of the end plate and the loading plates or small movement in the swivel joints can also reduce the initial stiffness of the specimen. In general, the FEM models are expected to be stiffer than the physical models.

The initial stiffness of both test specimens and the numerical model were calculated as secant stiffness at the 40% of the specimen strength and tabulated in Table 6. The average of the test to FEM stiffness for all specimens is 0.83 and the coefficient of variation is around 14%. The decrease in the test initial stiffness can also be justified by the high stiffness demand of the short specimens on the end plates and the clamps. As the failure of the specimen is a function of the force equilibrium and stress distribution on the cross section, any decrease in the initial stiffness may not affect the strength magnitude, although the failure may happen at a larger displacement.

Comparison of the tangent stiffness across the full history of the tests (Torabian et al. 2013) shows generally good agreement for the model, despite the slightly high initial stiffness.

Table 5: Failure modes in non-principal axes

	Bi-axial bending			
	(+) minor axis bending	(+) minor axis bending	(-) minor axis bending	(-) minor axis bending
	θ_{MM}=29.8°, ϕ_{PM}=74.2°	θ_{MM}=60.7°, ϕ_{PM}=75.1°	θ_{MM}=299.0°, ϕ_{PM}=74.8°	θ_{MM}=330.2°, ϕ_{PM}=74.2°
Experiment / Deformed Shaped	FDB	FDB	WLB	WLB
FEM	(L-) (D-)	(L-) (D-)	(L-) (D-)	(L-) (D-)

Table 6: Results summary: test results, finite element results and AISI-S100-12 strength predictions

No.	Bending Axis	Specimen in the test	Measured Angles		@ Peak load Eccentricities		Angles		Test result		AISI-S100-12	FEM result		Comparison		
			θ_{MM}	ϕ_{PM}	e_x	e_z	$\theta_{MM\text{-}peak}$	$\phi_{PM\text{-}peak}$	K_{Test}	β_{Test}	$\beta_{n\text{-}AISI}$	K_{FEM}	β_{FEM}	$\beta_{Test}/\beta_{n\text{-}AISI}$	K_{Test}/K_{FEM}	β_{Test}/β_{FEM}
			(deg.)	(deg.)	(in.)	(in.)	(deg.)	(deg.)	(kips/in.)	-	-	(kips/in.)	-	-	-	-
1		S600-12-1	270.0	79.8	-0.002	-1.268	270.0	81.4	138.1	1.40	0.69	167.2	1.20	2.03	0.83	1.17
2		S600-12-19	270.0	70.4	-0.003	-0.657	270.0	73.8	414.2	1.20	0.60	446.0	1.01	2.00	0.93	1.20
3	Minor	S600-12-4	270.0	43.8	0.001	-0.253	270.0	52.9	877.5	0.71	0.48	975.8	0.64	1.48	0.90	1.11
4		S600-12-5	90.0	29.4	0.001	0.113	90.1	30.7	986.5	0.69	0.47	1122.3	0.68	1.47	0.88	1.02
5		S600-12-6	90.0	58.0	0.001	0.398	90.0	64.3	730.0	0.94	0.60	802.4	0.78	1.56	0.91	1.21
6		S600-12-8	90.0	78.5	-0.005	1.064	90.0	79.8	225.5	1.22	0.80	216.9	0.94	1.51	1.04	1.30
7		S600-12-9	340.1	33.0	-1.009	-0.057	334.3	34.5	806.1	0.54	0.41	985.7	0.52	1.32	0.82	1.04
8	Major	S600-12-10	358.2	65.0	-3.518	-0.020	357.2	65.1	287.5	0.66	0.55	354.9	0.68	1.21	0.81	0.98
9		S600-12-11	360.0	77.7	-7.541	-0.006	359.6	77.8	52.2	0.80	0.69	100.5	0.80	1.16	0.52	1.00
10		S600-12-2	31.1	47.0	-1.512	0.123	34.7	48.4	605.1	0.61	0.43	803.1	0.60	1.41	0.75	1.01
11		S600-12-13	29.8	74.2	-5.021	0.386	33.2	74.8	152.4	0.67	0.54	186.8	0.74	1.23	0.82	0.90
12		S600-12-14	60.1	44.9	-0.821	0.205	64.8	49.8	735.5	0.67	0.45	943.7	0.68	1.50	0.78	0.99
13	Bi-Axial	S600-12-15	60.7	75.1	-3.017	0.736	64.3	76.8	237.2	0.90	0.59	253.0	0.86	1.53	0.94	1.05
14		S600-12-16	300.8	44.2	-0.819	-0.210	294.6	50.3	787.4	0.63	0.42	924.6	0.61	1.50	0.85	1.04
15		S600-12-17	299.9	74.8	-3.015	-0.704	296.7	76.3	188.9	0.93	0.52	253.7	0.91	1.79	0.74	1.01
16		S600-12-3	330.5	46.5	-1.511	-0.131	323.5	49.0	581.0	0.61	0.41	797.5	0.57	1.48	0.73	1.07
17		S600-12-20	330.2	74.2	-5.019	-0.376	327.4	74.7	151.5	0.78	0.51	186.1	0.79	1.54	0.81	0.99
											Average			1.51	0.83	1.06
											Standard deviation			0.24	0.11	0.10
											C.O.V			15.9%	13.6%	9.6%

3.2.3 Strength Interaction Surfaces

The physical test results, AISI-S100-12 predictions, and nonlinear material and geometric finite element results at the peak load are summarized in Table 6. The FEM results are compared to the test results to validate the numerical models, and the specification predictions are compared to test results to evaluate the current AISI-S100-12 specification for beam-column strength prediction. To be consistent with the definitions in P-M_1-M_2 space and to use the same parameters in all methods, all results are expressed in the θ_{MM}-ϕ_{PM}-β coordinate, where $\theta_{MM-peak}$, $\phi_{PM-peak}$ and β_{Test} were estimated at the peak load in the physical tests and the corresponding β_{FEM} and β_{n-AISI} where determined along the line associated with the $\theta_{MM-peak}$ and $\phi_{PM-peak}$.

The average β_{Test}/β_{FEM} is 1.06 and the associated C.O.V is 10%, indicating the FEM models are in reasonable agreement with the test results and the finite element model can be effectively used to predict the strength of beam-columns and extend the experimental results to the other eccentricities in the P-M_1-M_2 space.

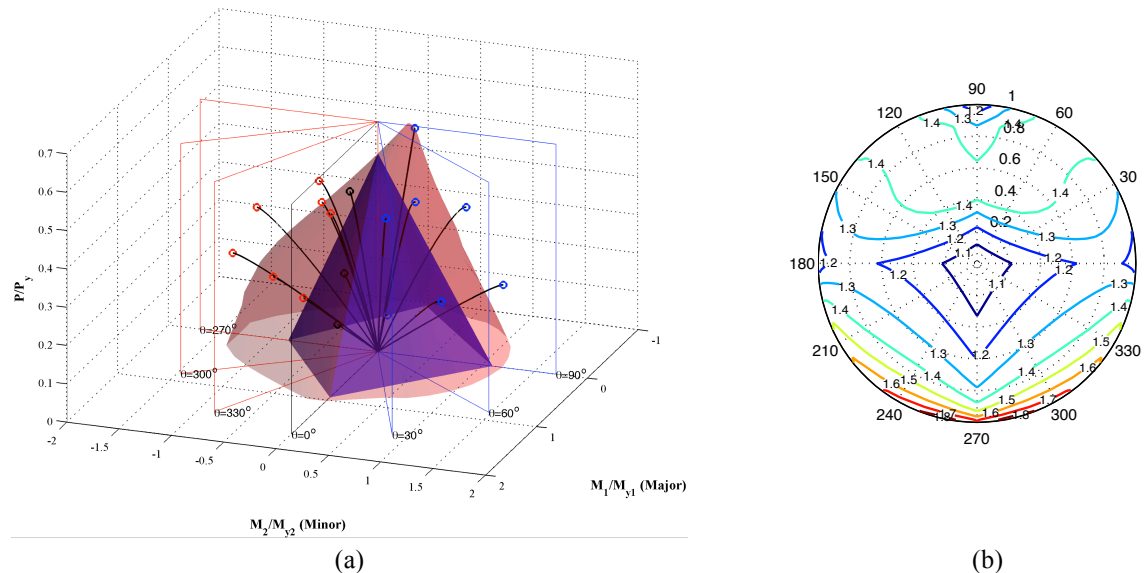|	
(a)	(b)

Figure 13: (a) Strength surfaces in P-M_1-M_2 space: Test results (line results), AISI-S100-12 nominal strength surface (blue surface), FEM strength surface (red surface); (b) $\beta_{FEM}/\beta_{n-AISI}$ contours: polar angle = θ_{MM}, radius = $\sin(\phi_{PM})$

Fig. 13(a) compares the AISI-S100-12 nominal strength surface to the FEM strength surface, which was verified to the test results and reliably simulates the test results for the complete P-M_1-M_2 space. The FEM strength surface was constructed base on the results of 343 collapse analyses with different eccentricities. The eccentricities were associated with 10° step in azimuth angle θ_{MM} and 5° step in the elevation angle ϕ_{PM}.

As shown in the figure, the specification strength surface is completely inside the FEM strength surface, thus showing that the specification provides conservative results for the entire P-M_1-M_2 space. To quantify the magnitude of the conservative prediction, the volume under of the FEM strength surface was calculated and divided by the volume under the AISI-S100-12 surface. The volumetric ratio of FEM to the code strength surface was estimated to be 1.32. To show the spatial distribution of the FEM over AISI predictions ($\beta_{FEM}/\beta_{n-AISI}$), the distribution is mapped to

a polar coordinate system as a contour plot as shown in Fig. 13(b). The specification predictions around the compression load anchor point provided the best prediction, while the minor axis bending predictions where the lip is in tension (θ_{MM} =270°) show the poorest prediction.

5. Summary and Conclusions

Testing to study cold-formed steel beam-columns is fully developed and shown to reliably and efficiently produce beam-column capacities for axial load (P) and major (M_1) and minor (M_2) axis bending. A lipped channel, 600S137-54 (345MPa [50 ksi]) at the length of 305 mm [12 in.], is specially selected and tested under a variety of P-M_1-M_2 loading. It is found that the current AISI-S100-2012 specification predictions for the beam-column strength of this section are quite conservative. Capacities developed under axial load and minor axis bending deviated considerably from expected. A shell finite element model is validated against the testing and implemented as a reliable means to expand the predicted performance of the beam-columns in the complete P-M_1-M_2 space. The results show the enormous potential for improving the current specification methods for beam-column design. Accordingly, a new Direct Strength Method for beam-columns that directly incorporates stability under the actual applied P-M_1-M_2 action and inelastic reserve in bending is underway and future improvements are desired. Work on additional testing on longer specimens and different cross sections, including parametric studies with the developed finite element collapse model, and user-friendly computational design tools, are also ongoing.

References

Moen, C.D., Igusa T., Schafer B.W. (2008). "Prediction of residual stresses and strains in cold-formed steel members", *Thin Wall Struct*, 46, 1274-1289.

Moen, C.D. (2008). "Direct strength design for cold-formed steel members with perforations." Ph.D. *Thesis, Johns Hopkins University*, Baltimore.

NAS. (2012). "North American Specification for the design of cold-formed steel structural members." Washington (DC, USA): *American Iron and Steel Institute*.

Li, Z., Schafer, B.W. (2010). "Application of the finite strip method in cold-formed steel member design." *Journal of Constructional Steel Research*, 66, 971–980.

Sarawit, A. (2006) "CUTWP thin-walled section properties", December 2006 update. (http://www.ce.jhu.edu/bschafer/cutwp).

SFIA (2012). "Technical Guide for Cold-Formed Steel Framing Products." *Steel Framing Industry Association*

Schafer, B.W., Adany S. (2006). "Buckling analysis of cold-formed steel members using CUFSM: Conventional and Constrained Finite Strip Methods. *Eighteenth international specialty conference on cold-formed steel structure.* Orlando, FL, United States: University of Missouri-Rolla, Rolla, MO, United States. (http://www.ce.jhu.edu/bschafer/cufsm)

Schafer, B.W., Li, Z., Moen, C.D. (2010). "Computational modeling of cold-formed steel." *Thin Wall Struct*, 48, 752-762.

Simulia. (2013). ABAQUS 6.13. (www. Simulia.com).

Standards Australia. (2005). "Cold-formed steel structures." NZS 4600, Sydney, Australia.

Torabian S., Zheng B., Schafer B.W. (2013). "Direct Strength Prediction of Cold-Formed Steel Beam-Columns", *Thin-walled Structures Group at The Johns Hopkins University. American Iron and Steel Institute (AISI).* (http://www.ce.jhu.edu/bschafer/dsmbeamcol/)

Zeinoddini, V. M., Schafer, B.W. (2012). "Simulation of geometric imperfections in cold-formed steel members using spectral representation approach". *Thin-Walled Structures*, 60, 105–117.